


# Silver Columnar Thin-Film-Based Half-Wavelength Antennas for Bright Directional Emission from Nanodiamond Nitrogen-Vacancy Centers

Rajesh Kumar,<sup>1,\*</sup> Faraz A. Inam,<sup>2</sup> Anh Ly,<sup>3</sup> Carlo Bradac,<sup>3</sup> and S. Anantha Ramakrishna<sup>1</sup>

<sup>1</sup>*Department of Physics, Indian Institute of Technology Kanpur, Kanpur 208016, India*

<sup>2</sup>*Department of Physics, Aligarh Muslim University, Aligarh 202002, India*

<sup>3</sup>*School of Mathematical and Physical Sciences, University of Technology Sydney, Ultimo, New South Wales 2007, Australia*

 (Received 1 July 2018; revised manuscript received 18 December 2018; published 1 March 2019)

Nitrogen-vacancy (N-V) centers in nanodiamond (ND) are a promising single-photon-source candidate for quantum technology. However, the poor N-V emission rate and low outcoupling of light significantly hinder their effective use in practical implementations. To overcome this limit, we place NDs hosting N-V centers on silver columnar thin films (CTFs) and measure an increase in emission by an order of magnitude. The CTFs consist of silver nanocolumns the length of which is chosen to be half the wavelength of the emitted light. The silver nanocolumns act as efficient optical antennas that couple to the N-V centers via the optical near field and outcouple the excitation energy of the N-V centers effectively into the optical far field. A large distribution of radiated powers from different NDs is observed. Computer simulations show this distribution to arise from the different orientations of the emitting dipoles with respect to the columnar axis. We also report that further structuring of the silver CTF into gratings yields higher photon emission.

DOI: [10.1103/PhysRevApplied.11.034002](https://doi.org/10.1103/PhysRevApplied.11.034002)

## I. INTRODUCTION

Single-photon sources are one of the most critical components of quantum information processing [1] and quantum cryptography [2]. The desirable requirements for single-photon sources include stable emission, a high photoemission rate, and, ideally, angularly confined emission [3]. Nitrogen-vacancy (N-V) centers in nanodiamond (ND) are promising single-photon-source candidates, as they possess stable emission even at room temperature [4]. They are, however, limited by a long radiative lifetime due to poor index matching at the diamond-air interface, which results in low emission rates [5]. Several methods have been suggested to outcouple the emission more efficiently; for instance, via coating with higher-refractive-index materials [6,7], near-field coupling to plasmonic and photonic structures [5,8–12], waveguides [13–15], tapered optical fibers [16], and fiber tips [17]. Also, anisotropic metamaterials [18] with hyperbolic dispersion have been used, as they have a divergent photonic localized density of states (LDOS), which can enhance the emission of N-V centers in NDs [19].

Atoms and molecules are very inefficient emitters due to their small subwavelength size [20]. Embedding them in a larger scattering structure such as a spherical nanodiamond

can increase the spontaneous emission intensity. Nevertheless, diamond nanoparticles are also subwavelength in size, which intrinsically inhibits large-scale enhancement. The impedance mismatch due to the large refractive index of diamond also hinders the N-V emission. Further, the radiation pattern of a small spherical nanoparticle is typically dipolelike [21] and does not display sufficient angular selectivity. In this context, a linear antenna of length ( $l$ ) smaller than the wavelength can emit radiation proportional to  $(l/\lambda)^3$  (the Wheeler limit) [22]. The antenna geometry critically determines the emission rate and radiation pattern and its length can severely impact the radiation. To produce large emission, the ideal length of an antenna should be about half the wavelength ( $\lambda/2$ ) of the emitted light. Thus, it would be desirable to couple the N-V in ND to  $(\lambda/2)$ -sized antennas in the near field to create enhanced outcoupling of the emission, as well as to provide directional output.

In this work, we place irradiated NDs hosting multiple N-V centers in silver columnar thin films (CTFs). We find that the N-V emittance (the measured photon count rates) is enhanced by about an order of magnitude when the CTF-nanocolumn length is about 350 nm (approximately half the wavelength of the central peak of the N-V emission spectrum, at about 680 nm). The silver CTF is essentially an anisotropic dielectric medium with hyperbolic dispersion [23]. By numerical simulations, the nanodiamond N-V

\*kraj@iitk.ac.in

is treated as a dipole emitter embedded in the nanostructured columnar medium. We find that the emittance is enhanced due to the nanocolumns acting as efficient optical antennas. The emittance from a large set of nanodiamond emitters in CTF is measured by confocal microscopy. The study reveals a wide distribution of measured photon count rates from N-V centers on a given substrate [24]. The presence of the silver nanocolumns shifts the entire measured count-rate distribution to higher values with a mean and median increased by roughly one order of magnitude. Detailed simulations reveal that similar distributions arise due to the different orientations of the emitting dipole in the ND with respect to the nanocolumn axis and the consequent difference in coupling. Autocorrelation studies confirm that the NDs used in the experiments contain multiple N-V centers. Further structuring of the silver CTF into grating structures results in marginal enhancement in the measured count rates as compared to that for the unpatterned CTF. Occasionally, emitters with relatively higher measured count rates are observed on the CTF gratings. These studies demonstrate the enormous potential of plasmonic CTF for developing efficient sources using N-V centers in NDs.

## II. SAMPLE PREPARATION

Silver columnar thin films (CTF) are deposited on glass (fused silica) and silicon substrates, with and without photoresist gratings, by evaporation of silver at large oblique angles. The one-dimensional gratings of photoresist (ma-P 1205) are made by laser interference lithography (LIL) [25] at a wavelength of 442 nm over an area of about 20 mm<sup>2</sup>. One-dimensional gratings with pitches of 500, 600, 700 and 800 nm are prepared. Gratings of different periodicity are used as substrates to deposit the CTFs. A collimated flux of silver is directed onto the substrate, cooled by a Peltier cooler to about  $-20^{\circ}\text{C}$ , at an angle of  $80^{\circ}$  with respect to the substrate normal, in a vacuum of  $5 \times 10^{-6}$  mbar. Random nucleation sites are formed in the initial film growth which, by shadowing the regions behind them, result in the columnar morphology of the thin film [26]. The deposition rate is maintained at  $15\text{--}19 \text{ \AA s}^{-1}$  and monitored using a quartz crystal monitor. Oblique angle deposition of a collimated flux of silver vapor on flat silicon (100) substrates yields forests of randomly distributed but highly oriented nanocolumns of silver, as shown in Fig. 1(a). Comparatively, deposition on linear gratings of a polymer yields a periodic array of oriented nanocolumns, as shown in Fig. 1(b). The nanocolumns have diameters of  $(40 \pm 5)$  nm and a length of about  $(350 \pm 10)$  nm. It is apparent from the cross-section view in the inset of Fig. 1(b) that the nanocolumns grow uniformly only from the ridges of the grating. We also note that some of the nanocolumns merge into one another due to the finite collimation of the silver vapor as well

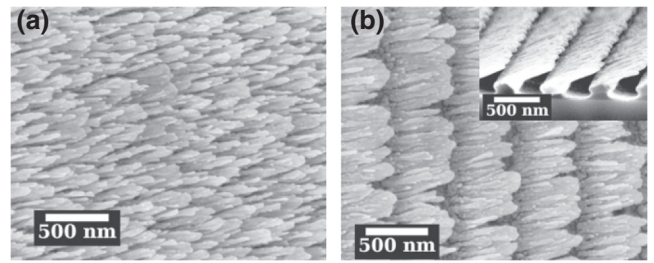


FIG. 1. (a) The top view of a field-effect scanning-electron-microscopy (FESEM) image of Ag CTF on silicon substrate. (b) The top view of a FESEM image of Ag CTF on a 500-nm PR grating. The inset shows the cross-section view.

as the finite deposition rate [26]. Regardless, the variation in column diameter is minor and the nanocolumn alignment is uniform across the sample. Notably, the tilt of the nanocolumns with respect to the substrate, the length of the nanocolumns, and the density and period of the grating are all variables that can be optimized to maximize the emission from the nanodiamond N-V centers.

Plain silver films are also deposited on the glass substrate and on photoresist gratings with different pitches by physical vapor deposition at normal incidence. A flux of silver in vacuum at  $7 \times 10^{-6}$  mbar is normally directed onto the samples at a low deposition rate  $0.7\text{--}1.5 \text{ \AA s}^{-1}$ . A  $25\text{-}\mu\text{l}$  aqueous solution of NDs is spin coated on silver CTF samples and the glass substrate at 3000 rpm, for 1 min. The same conditions are used for all the samples.

## III. CHARACTERIZATION AND MEASUREMENT

The fabricated CTF samples are imaged using field-effect scanning electron microscopy (FESEM) (BP 40 SUPRA, Carl Zeiss instruments). Figure 2 shows the top view of the FESEM image of nanodiamonds deposited on different silver CTF samples. The NDs are highlighted by a red circle. The images show that the NDs are located on the tip of the silver CTF and that they are also isolated from other NDs. It is evident from the FESEM images that the morphology of silver CTF does not change or get damaged by the spin coating of the solution of NDs on top.

An atomic-force microscope (XE70, Park Systems, South Korea) is used to determine the grating period and surface topography of the different samples. Figure 2(f) shows the surface topography of a plane silver film on the glass substrate. The film has a typical root-mean-square (rms) roughness of approximately 3.5 nm, as measured from the line profile in the inset of Fig. 2(f).

Optical characterizations are performed using a commercial confocal microscope (alpha300 S, WITec, Germany). A schematic diagram of the experimental setup of the confocal fluorescence microscope is shown in Fig. 3. A 532-nm continuous-wave (cw) diode laser is used to

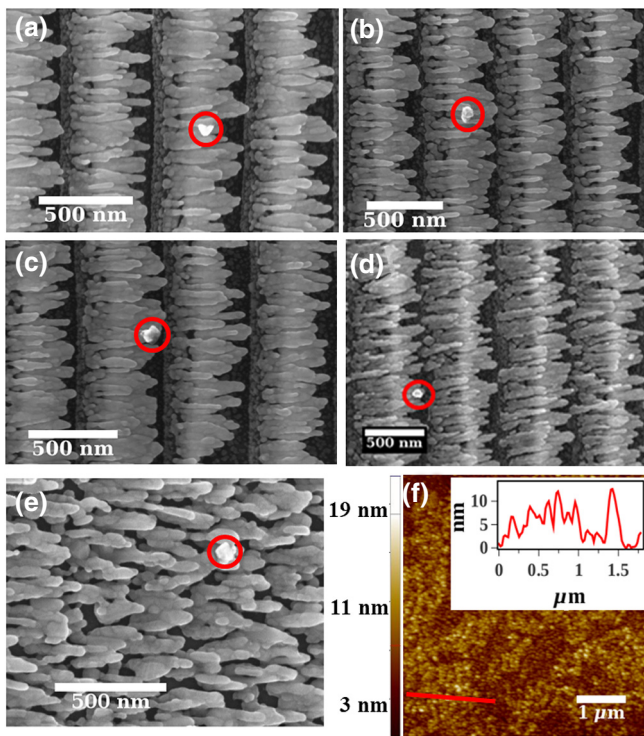


FIG. 2. The top view of a FESEM image of ND deposited on a 500-nm-periodicity silver CTF at three different locations (a)–(c), on a 600-nm-periodicity silver CTF (d), and on an unpatterned silver CTF (e). (f) An atomic-force-microscopy (AFM) image of the surface topography of the silver-film-coated sample, over an area of  $5 \times 5 \mu\text{m}^2$ ; the inset shows the line profile of the film.

excite the N-V centers in the NDs. The laser beam is coupled to the microscope by a single-mode optical fiber. A  $100\times$  objective with a numerical aperture (NA) of 0.75 is used to focus the light onto the sample. Fluorescence is collected from the NDs using the same objective, through a 532-nm notch filter and directed to an avalanche photodiode (APD) for detection in photon-counting mode. Lifetime measurements of the ND N-V centers are carried out using a laboratory-built confocal microscope with a  $100\times$  objective and a 0.9 NA and a Fianium White-Lase excitation laser source (532 nm wavelength, 10 MHz repetition rate, and  $10 \mu\text{W}$  excitation power).

The N-V emission spectrum from a nanodiamond on a glass substrate and on an Ag CTF sample is presented in Fig. 4(a), which clearly shows the zero-phonon line (ZPL) at 637 nm, along with the typical broad-phonon side band at higher wavelengths. The fluorescence confocal images of the emission from N-V centers in NDs on a glass substrate and on a 500-nm Ag CTF grating are shown in Figs. 4(b) and 4(c), respectively. While some clusters of emitting NDs are present, only isolated centers with a diffraction-limited fluorescence spot [see the insets in Figs. 4(b) and 4(c)] are considered in the photoemission measurements. The scanning-electron-microscope (SEM)

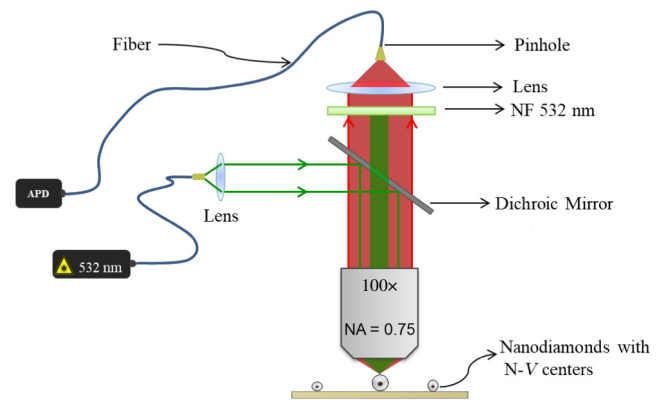


FIG. 3. A schematic diagram of the experimental setup of the confocal fluorescence microscope. NF 532 nm, notch filter to cut off the 532-nm excitation light; APD, avalanche photodiode.

images of the nanodiamonds on CTF samples show that most of the diamond nanocrystals are located near the top end of the nanocolumns (Fig. 2). By measuring the N-V-center photon count rates, the emission from the individual ND N-V center on an Ag CTF is found to be typically enhanced by over an order of magnitude compared to the N-V emission from ND on the glass substrate—used as the reference control sample. A wide distribution in the N-V-center collected photon count rates on both the glass substrate and the CTF sample is observed and attributed to the arbitrary orientation and location of the N-V dipole within the diamond crystal [6]. A statistical study of the N-V-center emission on glass and various CTF substrates is carried out to measure the average influence of the different substrates on the N-V-center emission. For this, around 40 stable near-diffraction-limited emitters are studied on various substrates. The limited number of studied emitters may not result in a proper normalized distribution; however, the mean will vary only within the measured standard deviation. The distributions of the measured photon count rates from the NDs on various substrates are plotted in Fig. 5.

The emission from NDs on glass shows a broad distribution of measured count rates ranging from 0 to  $20 \times 10^3$  counts/s, with a mean of  $(9 \pm 5) \times 10^3$  counts/s and a mode of  $5 \times 10^3$  counts/s. For the NDs placed on the unpatterned silver film, the mean increases to about  $(46 \pm 29) \times 10^3$  counts/s, the mode to about  $20 \times 10^3$  counts/s, and there are a few centers with large count rates around  $100 \times 10^3$  counts/s. This enhancement is expected due to the plasmonic nature of the silver film as well as the surface roughness and it is comparable to previous reports for other emitters [27–29]. The structuring of the silver CTF into a gratinglike structure does not seem to affect the distribution of emissions in a notable way. When the NDs are deposited on a silver CTF, larger enhancements are observed, with the mean of the measured count rates

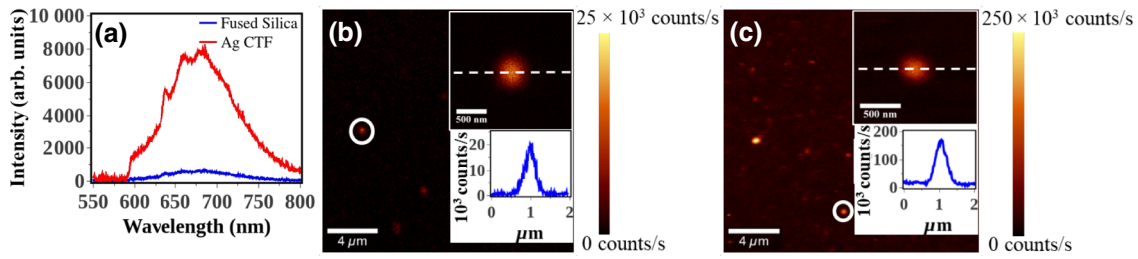


FIG. 4. (a) The  $N-V$ -center spectrum obtained from our ND samples, at room temperature. (b),(c) Confocal images of the fluorescence emission from ND  $N-V$  centers over an area of  $20 \times 20 \mu\text{m}^2$  on a glass substrate (b) and when placed on the Ag CTF 500-nm grating sample (c). The confocal scan of a single emitting ND is shown in the top inset of both figures, over an area of  $2 \times 2 \mu\text{m}^2$ . The bottom inset shows the image intensity along the dashed line.

increasing to up to  $(70 \pm 53) \times 10^3$  counts/s and the mode to  $40 \times 10^3$  counts/s, with measured count rates of up to  $200 \times 10^3$  counts/s from some emitters. Structuring the CTF further into a grating causes some of the embedded NDs to display even higher count rates. While the mean and the mode increase by only about 10%,  $N-V$  centers with very large measured count rates of up to and in excess of  $300 \times 10^3$  counts/s are observed. These occurrences are, however, infrequent and probably arise due to cavity-like resonances in the grating, as discussed below. While we observe a wide distribution of measured count rates in all cases, the distributions appear consistent within each sample, indicating a possible common origin. We attribute the

distribution of measured count rates and, in turn, of the emission rates to the different orientation of the radiating dipoles ( $N-V$  centers) relative to the substrate and the nanocolumnar axis.

A measure of the total decay-rate enhancement of the dipole emitter can be determined by measuring the corresponding reduction in the emitter’s lifetime. Figure 6(b) shows the distribution of measured lifetimes for nanodiamond  $N-V$  centers on Ag CTF and glass substrates. The results show the mean  $N-V$ -center lifetime on Ag CTF substrates to be nearly half [ $\tau = (13.5 \pm 2.5)$  ns] the value on the glass substrate [ $\tau = (20.4 \pm 4.8)$  ns]. This corresponds to an enhancement in the  $N-V$ -center total decay

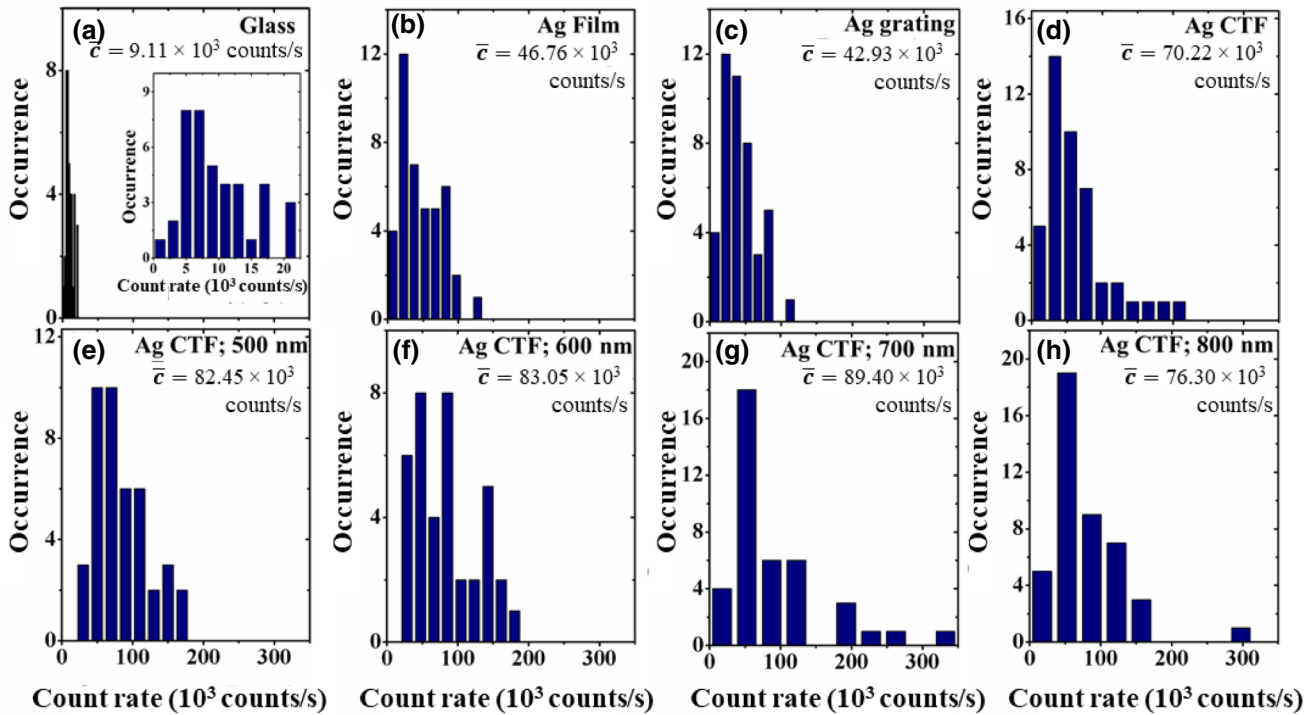


FIG. 5. The statistical distribution of the experimentally measured powers from  $N-V$  centers in ND placed on different surfaces: on a glass substrate (a), on a plain silver film (b), on a 600-nm silver grating (c), on an unpatterned silver CTF (d), and on a periodically patterned silver CTF with the period ranging from 500 to 800 nm (e–h), respectively.  $\bar{c}$ , Mean value.

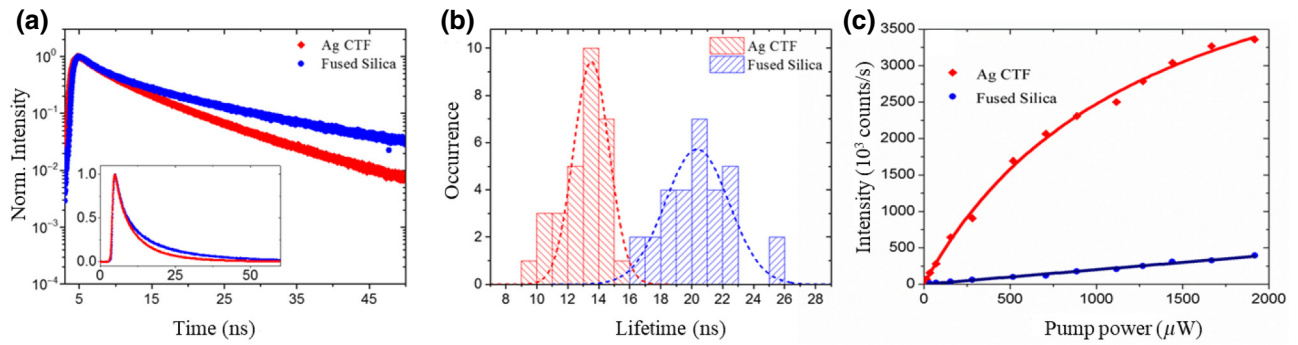


FIG. 6. (a) Lifetime decay curves for N- $V$ -center emission on Ag CTF (red) and glass (blue) substrates. (b) The corresponding lifetime distributions for N- $V$ -center emission on the two substrates. The average lifetime values are  $\tau = (13.5 \pm 2.5)$  ns for the Ag CTF sample and  $\tau = (20.4 \pm 4.8)$  ns for the glass sample, respectively. (c) The emission-intensity saturation curve for a nanodiamond on silver CTF (red) and for a reference nanodiamond on glass substrate (blue).

rate by roughly a factor of 2. The observed enhancement by one order of magnitude in photon count rates is therefore likely the result of the Ag CTF-nanocolumn antenna effect of directing the N- $V$  emission mainly toward the top, i.e., orthogonal with respect to the substrate plane.

The N- $V$ -center lifetime in bulk diamond is well known to be constant around 11.6 ns [30,31] due to a homogenous electrodynamic environment for all N- $V$ -dipole orientations in the bulk diamond. However, in subwavelength-size nanodiamond crystals, N- $V$  centers are known to have a large distribution in their range of emission lifetimes, from about 5 to 50 ns, with a mean of about 22–23 ns [6,32,33]. The distribution results from various factors including the N- $V$  dipole's proximity and its orientation relative to the air-glass (substrate) [6,34,35] and the irregularity in the crystal geometry for crystal sizes in the subwavelength regime [6,33] as well as being due to the large distribution in the quantum efficiencies of individual N- $V$  centers in the ND [24,36]. For N- $V$  dipoles with variable quantum efficiencies, the suppression in the local density of states (LDOS) due to the Lorentz-Lorenz effect [37] in subwavelength highly dielectric diamond crystals will also show a significant variation [36,38], leading to a large distribution of the emission rates. Further, in the case of our study, a distribution in the emission rates and the radiated powers is also expected to arise due to the presence of multiple N- $V$  centers within a ND. Since each ND is hosting a variable number of N- $V$  centers, the variation in the number of N- $V$  centers in each ND will lead to a distribution in the radiated powers.

Fluorescence counts from photostable single nanodiamond deposited on silver CTF and glass are measured as a function of different incident powers of a 532-nm continuous-wave diode laser. The power saturation of the nanodiamond emission with respect to the incident excitation power, when placed on silver CTF and glass substrate, is shown in Fig. 6(c). Here, the power shown on the  $x$  axis of the graph is the excitation laser power measured at

the output end of the single-mode optical fiber just before coupling to the back of the microscope objective. A neutral density filter is placed in the collector to avoid saturation of the avalanche-photodiode (APD) detector. Therefore, the measured photon count rates shown in Fig. 6(c) are relative. The measured photon count rates increase almost by an order of magnitude in the case of the silver CTF sample as compared to the N- $V$ -center emission on the glass substrate. The N- $V$  emission of the silver CTF also appears to reach the saturation level at a lower power compared to the case of its emission on the reference glass substrate. This may result from the localization of the excitation laser (532 nm) scattered field at the N- $V$ -dipole location due to the silver CTF.

The one-order-of-magnitude increase in the measured photon count rates indicates that the half-wavelength Ag CTF nanocolumns are acting as efficient antennas that direct the dipole radiated power along the top direction. Here, the nanocolumns are oriented at a small angle to the substrate surface, as shown in the inset of Fig. 1(b). The effectiveness of the half-wavelength Ag CTF-nanocolumn antennas can also be seen from the collected N- $V$  emission spectrum [Fig. 4(a)] on glass and CTF substrates, as well as from the power-saturation curves of the N- $V$  emission on glass and CTF substrates [Fig. 6(c)]. In all these cases, an enhancement of about an order of magnitude in the N- $V$ -center emission is observed.

For completeness, we also perform autocorrelation studies on the N- $V$  centers on various substrates. However, as our NDs are irradiated, we cannot observe any antibunching behavior from these samples due to the presence of multiple N- $V$  centers in each crystal. Since we use the same ND samples for all substrates including the glass, the Ag film, and the Ag CTFs, we expect that the influence of the substrate should remain the same even in the case of multiple N- $V$  centers. Also, a multiexponential decay behavior can be observed in the N- $V$ -center lifetime curves on different substrates [Fig. 6(a)]. As discussed above, individual

N- $V$  dipoles are expected to have different lifetimes due to the influence of multiple factors. The difference in the individual dipole orientations relative to the air-glass interface of the substrate will result in a distribution of lifetimes [34]. The variable proximity of the individual N- $V$ -center dipoles to the interface will also have an influence on its lifetime distribution [34]. The individual quantum efficiencies of the individual N- $V$ -center dipoles are also expected to be different [24]. The lifetime decay curves are therefore expected to have a multi-exponential behavior. Through numerical calculations, we can check and verify that in fitting a multiexponential curve by a single exponential fit, we get lifetimes close to the average lifetime of all the individual centers. Since we observe continuity in the N- $V$ -decay-curve fittings for the various substrates, we expect the average lifetime values to remain nearly the same in each case.

#### IV. NUMERICAL CALCULATIONS

A detailed computational study of the emission originating from a point electric dipole (N- $V$  center) in the ND, placed on various structures, is carried out using the finite-element method, implemented in the COMSOL MULTIPHYSICS® suite. The ND is taken to be a spherical particle with a diameter of 45 nm and a refractive index of 2.47. The silver CTF is modeled as an array of prolate silver ellipsoids inclined at 25° on a dielectric substrate (photoresist with a refractive index of 1.62). The Lorentz-Drude model is used to describe the dielectric permittivity of silver with a plasma frequency of 2180 THz and damping of 5.0778 THz [39]. Clumps of two or three nanocolumns on the grating ridge are considered in a unit cell, similar to the FESEM images in Fig. 1. The geometrical parameters of the CTF are obtained from the cross-section FESEM image shown in Fig. 1(b), i.e., length  $350 \pm 10$  nm and diameter  $40 \pm 5$  nm. Floquet boundary conditions are used in the  $y$  direction and a perfect matching layer (PML) is used at the boundaries along the  $x$  direction. The distance between two nanocolumns along the  $y$  direction is considered to be 5 nm. The nanocolumnar axis is set to lie in the  $x$ - $z$  plane. The drive frequency of the dipole source corresponds to the peak emission wavelength, 680 nm.

##### A. Length optimization

The nanocolumnar length is optimized numerically to obtain the maximum emission rates. The effect on the coupling of the dipole emission due to a different orientation with respect to the nanocolumn axis is also analyzed. The nanodiamonds are considered to be at the tip of the nanocolumn. To have a comparison of the measured power for the nanodiamond N- $V$ -center emission on various substrates, the power radiated by the point electric dipole in the upward direction is calculated by integrating the  $z$

component of the time-averaged Poynting-vector flux over a flat surface at 300 nm above the dipole. Figure 7(a) shows the dipole radiated powers on the top surface for different nanocolumnar lengths corresponding to the three perpendicular dipole orientations. The nanocolumnar diameter is considered to be 45 nm. There is a large variation in the emission rate in the proximity of the 400 nm length of the nanocolumn when the dipole is oriented along the  $z$  direction. The emission rate is also close to a maximum at the 400-nm value for the length of the nanocolumn for a dipole orientation along the  $x$  and  $y$  directions. The emission rates are large for a nanocolumnar length in the range 350–450 nm.

The simple Ag nanocolumns used here are essentially a form of dipole antenna, the antenna modes being dipolar resonances [40]. The coupling of the dipole radiation fields to the antenna modes should be sensitive to the dipole orientation relative to the Ag antenna. For effective coupling, the wave vectors of the point-dipole radiation pattern should be matched with the resonance modes of the Ag nanocolumn antenna. This coupling is expected to be a maximum for an emitter-dipole orientation perpendicular to the Ag-nanocolumn antenna surface. In this case, the wave vectors of the emitter-dipole radiation field will be along the nanocolumn surface and will effectively couple to the radiation modes of the Ag-nanocolumn-dipole antenna. In Fig. 7(c), the top-radiated power is calculated for the different dipole orientations in the  $x$ - $z$  plane. It can be observed from the figure that the maximum top-radiated power is achieved when the dipole is oriented perpendicular to the nanocolumnar axis. Figure 7(d) shows the top-radiated power from a point electric dipole in a ND placed on a glass substrate for the different dipole orientations in the  $x$ - $z$  plane. In this case also, the maximum power is observed when the dipole orientation is perpendicular to the glass substrate. Dipoles oriented perpendicular to the interface are known to experience the highest spontaneous emission rates [34]. In the case, the air-glass interface itself is known to act as an antenna, directing most of the radiated power along the vertical directions [34]. The same size for the unit cell is used in both cases for comparison.

Figure 7(e) shows the normalized scattered electric field close to the tip of the silver CTF nanorod as a function of the excitation wavelength. The  $p$ -polarized (electric-field vector along the glass surface) plane wave at normal incidence is used for excitation. The normalized scattered electric field is calculated at the location of the point dipole in the nanodiamond. The figure shows that there are two resonances at 550 nm and 640 nm, which are very close to the excitation field and the zero-phonon line of the N- $V$  emission, respectively. This indicates that both the excitation field and the emission are enhanced due to the intense local electric field [12] of the silver CTF and the presence of the two broad resonance peaks.

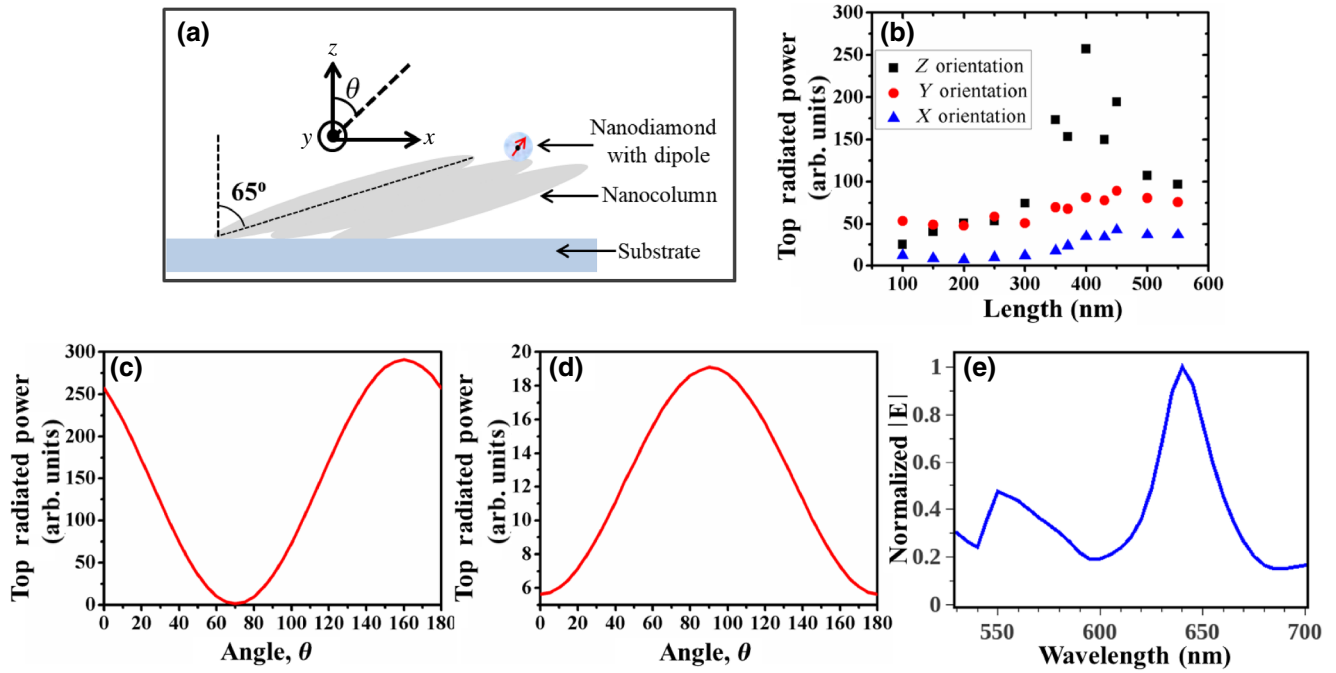


FIG. 7. (a) A schematic diagram of a silver CTF with ND on the tip of the nanocolumn. (b) The top-radiated power of the point electric dipole in the nanodiamond placed near the tip of nanocolumns with different lengths, for three orthogonal dipole orientations. The top-radiated power with respect to the dipole orientation in the  $x$ - $z$  plane (c) when the dipole is placed near the tip of the nanocolumn with 400-nm length and (d) when dipole is placed on the glass substrate. (e) The absolute value of the normalized electric field as a function of the wavelength, calculated at a point close to the tip of the nanorod.

### B. Statistical study of the emission rates

We computationally perform a statistical study of the emission from the  $N-V$  centers in ND on the different substrates. Dipoles with 100 different orientations and locations within the diamond nanocrystal are randomly chosen for the statistical study of the top-radiated powers. The distributions of the calculated powers on different substrates are shown in the top panels Figs. 8(a)–8(d), where a common unit-cell size is used in all cases to enable direct comparison. To compare with the experimental measurements, the ratio of the experimental mean photon collection rate to the calculated mean power in the case of NDs on a glass substrate is used as a common factor to scale all the other calculated results. For comparison, the corresponding histogram plots from the experiment are included in the bottom panel of Fig. 8. The range of top-radiated powers calculated [Fig. 8(a), top] for the glass substrate is about the same as experimentally measured [Fig. 8(a), bottom], suggesting that the distributions mainly arise due to the random orientations of the dipoles. The top-radiated power distributions from the dipoles in ND on the silver film and on the 700-nm-period silver grating, in Figs. 8(b) and 8(c), show that the top-radiated power is enhanced, yet not as much as observed experimentally. The distribution of the powers, however, appears similar in both cases. The major contribution of the discrepancy in Figs. 8(b) and 8(c) to the experimentally measured values

is expected to arise due to the surface roughness of the silver film in the experiment. In simulation, the silver film is modeled as a flat smooth surface, leading to a discrepancy between the experiments and the calculations. Due to the surface roughness of the silver film, random plasmonic nanocavities (hot spots) are expected to be formed all along the surface. This will lead to enhanced radiated powers for dipole emission on the silver-film substrate.

The distribution of the radiated powers for the dipole in the ND on the silver CTF grating [Fig. 8(d), top] is large and appears very similar to the powers measured experimentally [Fig. 8(d), bottom]. Reassuringly, there are also rare cases where the measured power exceeds  $300 \times 10^3$  counts/s, with the mean and mode having values similar to those found in the experiments [Fig. 5(h)].

### C. Far-field calculations

The electromagnetic fields and the power flow in the system offer deep insight into the physical mechanisms. Figure 9(a) shows the  $x$  component of the electric field along with the streamline plot of the Poynting-vector field for the radiating dipole located at the top of the middle nanocolumn in a silver CTF. Figure 9(b) shows the same quantities when the ND is placed on a glass substrate. In the case of Fig. 9(b), the radiation flow is more isotropic, although the field is null in the normal direction due to the interference of the field emanating from the dipole and the

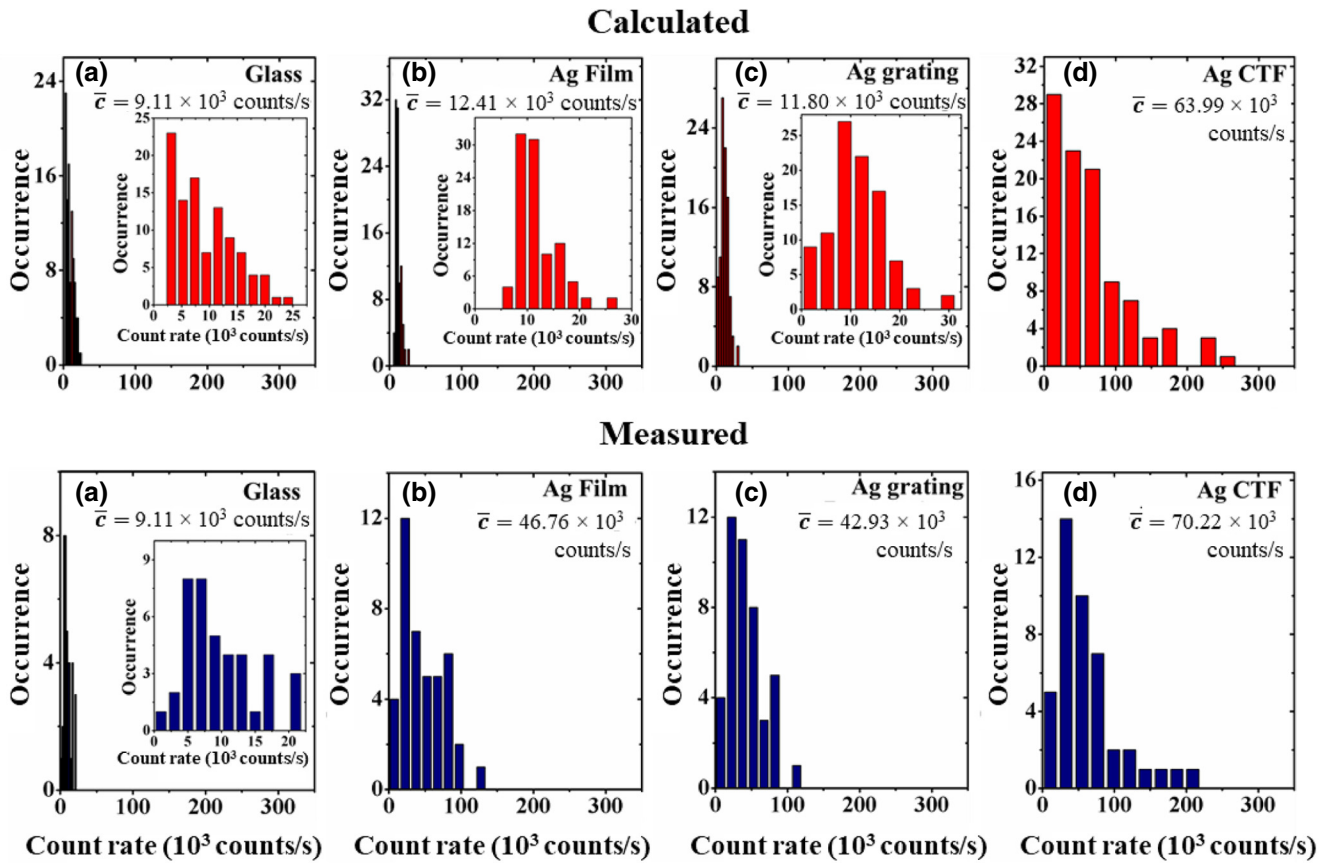


FIG. 8. Top: the statistical distributions of the computed top-radiated powers of a point dipole with a nanodiamond placed on different samples: (a) on a glass substrate, (b) on silver film, (c) on a 700-nm silver grating, and d) on a periodically patterned Ag CTF with a period of 700 nm. Bottom: the corresponding histogram plots from the experiment for comparison.

reflected dipole. This is consistent with the radiation from a small-sized dipole emitter [41]. When we look at the fields in the case of the dipole placed on the silver nanocolumns, we immediately note the presence of a resonant electromagnetic mode on the nanocolumns. These currents on the  $(\lambda/2)$ -sized nanocolumns radiate directionally, as clearly highlighted by the Poynting-vector maps. This directionality arises solely due to the strong coupling of the dipole fields to the nanocolumns in the near-field regime.

Polar plots of the far-field emission intensities for three orthogonal dipole orientations are shown in Fig. 10. Figures 10(a) and 10(b) show the polar plots of the far-field intensity in the  $y$ - $z$  plane when the dipole is placed on a glass substrate with its orientation along the  $x$  and  $z$  directions, respectively. Figures 10(c) and 10(d) show the polar plots of the far-field intensity in the  $y$ - $z$  and  $x$ - $z$  planes when the dipole is placed on the tip of the nanocolumn with its orientation along the  $x$  and  $y$  directions, respectively. The far-field radiation intensity pattern in the case of a dipole placed on the nanocolumn is quite different when the dipole is placed on the glass substrate. The main differences are that the emission is confined within a smaller angular range in the case of the dipole placed on the

CTF and that the intensity is enhanced, particularly for dipole orientations along the  $y$  and  $z$  directions [Figs. 10(c) and 10(e)]. For the dipole orientation along the  $z$  direction, there is an order-of-magnitude increase in the far-field intensity.

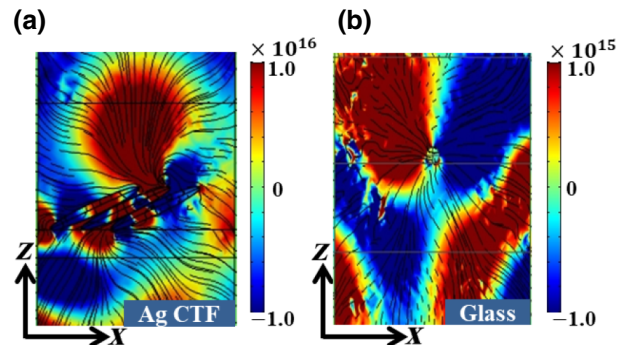


FIG. 9. (a) A color plot of the  $x$  component of the electric field along with streamlines showing the Poynting vector (power flow) of a radiating dipole in an ND sphere placed on the silver CTF. (b) The corresponding quantities for the dipole in an ND placed on the glass substrate.



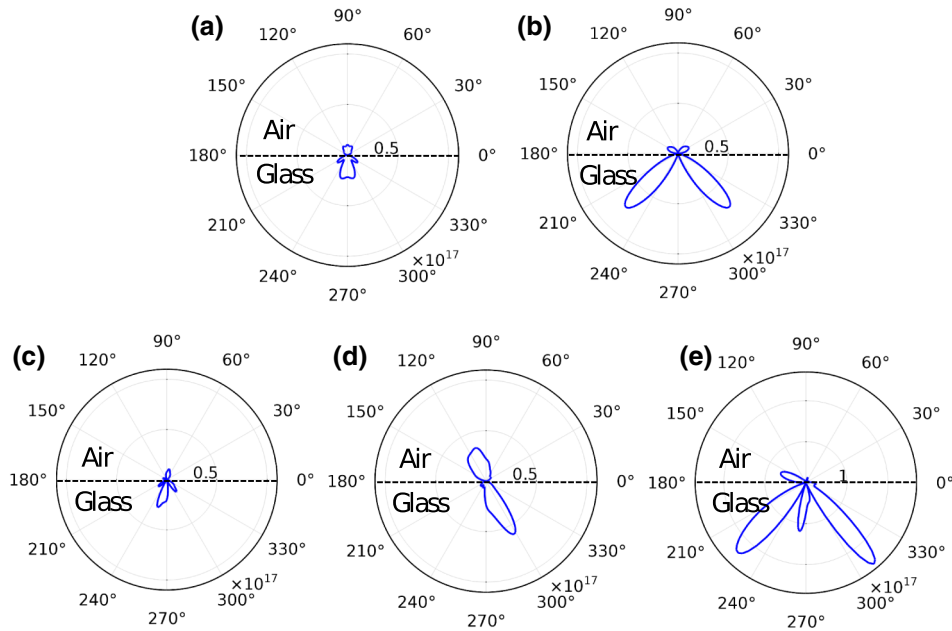


FIG. 10. Polar plots of far-field radiation intensity patterns: (a),(b) when an electric point dipole is placed on a glass substrate with its orientation along the  $x$  and  $z$  directions, respectively; (c)–(e) with orientations along the  $x$ ,  $y$ , and  $z$  directions, respectively, when placed on the tip of the nanocolumn, with the nanorod oriented in the  $x$ - $z$  plane. For comparison, (a)–(d) are plotted on the same scale. However, due to the relatively higher magnitude of the radiation intensities for (e), that figure is plotted on a higher scale.

## V. DISCUSSION

Overall, we observe that N- $V$  centers in NDs emit more efficiently and directionally in the presence of silver nanocolumns. The degree of enhancement is broad, which we attribute to the random spread of possible orientations of the dipole with respect to the nanocolumn axis. This evidence principally points to the fact that the nanocolumns act as efficient ( $\lambda/2$ ) antennas driven in the near field by the excited N- $V$  center. To put these results into context, we make the following working assumptions. We consider the nanodiamond N- $V$  centers to be radiative and highly quantum efficient [42]. The average quantum efficiency of N- $V$  centers in NDs is known to vary among individual centers [24], with an average value of about 0.7 for similar-sized ND crystals [33]. Since our confocal microscope is a commercial model that is not optimized for single-photon counting studies and has a lower collection efficiency with the objective lens numerical aperture (NA) of 0.75 (the detection efficiency of our confocal system is expected to be about 1% for dipole emission on top of the glass substrate), we expect to collect light from only bright emitters with higher quantum efficiencies. Other works studying N- $V$ -center spontaneous emission enhancement using plasmonic schemes have also considered the N- $V$  centers to have high quantum efficiency [42]. As the N- $V$  centers are embedded within the NDs and well protected, strong quenching effects due to the silver nanostructure are unlikely and therefore are not

considered in our analysis. While the enhancements in the case of NDs placed on the plane silver film are increased due the surface roughness, our simulations assume no surface roughness for the nanocolumns in the case of an ND placed on the CTF, thus explaining the slight discrepancy between simulations and experiments. The emission from the N- $V$  coupled to the larger length scale (approximately  $\lambda/2$ ) of the Ag CTF nanocolumns shows a one-order-of-magnitude enhancement in the emittance. A good match between the experimental and simulation results is found in this case. The surface roughness is expected to have minimal effects in this (approximately  $\lambda/2$ ) length-scale scenario. We thus attribute the effect seen here to the nanoantenna geometry rather than to the surface roughness, as in surface-enhanced fluorescence or surface-enhanced Raman scattering.

## VI. CONCLUSIONS

We measure a significant enhancement in the emission of N- $V$  centers in NDs placed on silver CTFs. The emittance is enhanced by about one order of magnitude compared to the emittance of nanodiamonds placed on a glass substrate. A wide variation of the measured photon count rates is shown to arise from the random orientation of the emitting dipoles with respect to the substrate or the silver nanocolumns. We show by computer simulations that the enhancement mainly arises from the coupling of the near-field radiation to the silver nanocolumns, which hence

act as efficient antennas, approximately  $(\lambda/2)$  in size. This is evidenced by the excitation of resonant modes on the nanocolumn. These enhancements are also related to the hyperbolicity of the silver CTF medium. Further structuring of the silver CTFs into gratings gives rise to a few cases in which much larger enhancements are observed, although the mean and mode of the distributions are not much different. These measurements show the interesting potential of combining these plasmonic CTFs with nanodiamond N-V centers in order to generate more efficient single-photon sources. The protection of the N-V centers from the external environment provided by the ND is still present while the optical nanoantenna offers the possibility of increased outcoupling. Careful design is expected to further enhance the capabilities of these devices. For example, it is found that dipole orientations normal to the CTF produce the largest emission rates. We note that CTFs, having columns with smaller inclination angles to the substrate, give rise to large normal fields in the gap between the substrate and the inclined nanocolumns [12,43]. These configurations may be further utilized to enhance the N-V emission.

In conclusion, we measure about an order-of-magnitude enhancement in the emittance from NDs hosting N-V centers by simply drop-casting the solution containing the NDs in deionized water on top of the silver CTFs. Alternatively, using sophisticated fabrication techniques, nanophotonic resonator structures have been fabricated within the bulk diamond crystal, including diamond nanopillars [4], diamond parabolic reflectors [44], or monolithic tunable optical cavities [45]. These nanophotonic resonators have resulted in significantly large emission enhancement, with an increase of up to about 2 orders of magnitude in the radiated powers from the diamond-based N-V centers or the silicon-vacancy (Si-V) centers. These schemes are mostly restricted to color centers embedded inside the bulk diamond crystal. In contrast, our scheme is applicable to vacancy centers embedded in diamond nanocrystals. Our results could inspire new directions toward the realization of all-solid-state single-photon sources for quantum-photonic applications.

### ACKNOWLEDGMENTS

R.K. thanks UGC India for the fellowship. We acknowledge the Department of Science and Technology (India) for funding under project Grant No. DST/SJF/PSA-01/2011-2012. C.B. is funded by an Australian Research Council Discovery Early Career Researcher Award (DE180100810) and a University of Technology Sydney Chancellor's Postdoctoral Research Fellowship.

---

[1] C. Monroe, Quantum information processing with atoms and photons, *Nature* **416**, 238 (2002).

- [2] A. Beveratos, R. Brouri, T. Gacoin, A. Villing, J.-P. Poizat, and P. Grangier, Single Photon Quantum Cryptography, *Phys. Rev. Lett.* **89**, 187901 (2002).
- [3] I. Aharonovich, D. Englund, and M. Toth, Solid-state single-photon emitters, *Nat. Photonics* **10**, 631 (2016).
- [4] T. M. Babinec, B. J. Hausmann, M. Khan, Y. Zhang, J. R. Maze, P. R. Hemmer, and M. Lončar, A diamond nanowire single-photon source, *Nat. Nanotechnol.* **5**, 195 (2010).
- [5] J. T. Choy, B. J. Hausmann, T. M. Babinec, I. Bulu, M. Khan, P. Maletinsky, A. Yacoby, and M. Lončar, Enhanced single-photon emission from a diamond-silver aperture, *Nat. Photonics* **5**, 738 (2011).
- [6] F. Inam, T. Gaebel, C. Bradac, L. Stewart, M. Withford, J. Dawes, J. Rabeau, and M. Steel, Modification of spontaneous emission from nanodiamond colour centres on a structured surface, *New J. Phys.* **13**, 073012 (2011).
- [7] A. Khalid, K. Chung, R. Rajasekharan, D. W. Lau, T. J. Karle, B. C. Gibson, and S. Tomljenovic-Hanic, Lifetime reduction and enhanced emission of single photon color centers in nanodiamond via surrounding refractive index modification, *Sci. Rep.* **5**, 11179 (2015).
- [8] J. T. Choy, I. Bulu, B. J. Hausmann, E. Janitz, I.-C. Huang, and M. Lončar, Spontaneous emission and collection efficiency enhancement of single emitters in diamond via plasmonic cavities and gratings, *Appl. Phys. Lett.* **103**, 161101 (2013).
- [9] M. Aramesh, J. Cervenka, A. Roberts, A. Djalalian-Assl, R. Rajasekharan, J. Fang, K. Ostrikov, and S. Praver, Coupling of a single-photon emitter in nanodiamond to surface plasmons of a nanochannel-enclosed silver nanowire, *Opt. Express* **22**, 15530 (2014).
- [10] A. Huck, S. Kumar, A. Shakoor, and U. L. Andersen, Controlled Coupling of a Single Nitrogen-Vacancy Center to a Silver Nanowire, *Phys. Rev. Lett.* **106**, 096801 (2011).
- [11] S. K. Andersen, S. Kumar, and S. I. Bozhevolnyi, Coupling of nitrogen-vacancy centers in a nanodiamond to a silver nanocube, *Opt. Mater. Express* **6**, 3394 (2016).
- [12] T. B. Hoang, G. M. Akselrod, and M. H. Mikkelsen, Ultrafast room-temperature single photon emission from quantum dots coupled to plasmonic nanocavities, *Nano Lett.* **16**, 270 (2015).
- [13] R. Rajasekharan, G. Kewes, A. Djalalian-Assl, K. Ganesan, S. Tomljenovic-Hanic, J. C. McCallum, A. Roberts, O. Benson, and S. Praver, Micro-concave waveguide antenna for high photon extraction from nitrogen vacancy centers in nanodiamond, *Sci. Rep.* **5**, 12013 (2015).
- [14] M. G. Harats, N. Livneh, and R. Rapaport, Design, fabrication and characterization of a hybrid metal-dielectric nanoantenna with a single nanocrystal for directional single photon emission, *Opt. Mater. Express* **7**, 834 (2017).
- [15] T. H. Taminiau, F. Stefani, and N. F. van Hulst, Single emitters coupled to plasmonic nano-antennas: Angular emission and collection efficiency, *New J. Phys.* **10**, 105005 (2008).
- [16] M. Fujiwara, K. Toubaru, T. Noda, H.-Q. Zhao, and S. Takeuchi, Highly efficient coupling of photons from nanoemitters into single-mode optical fibers, *Nano Lett.* **11**, 4362 (2011).
- [17] T. Schröder, A. W. Schell, G. Kewes, T. Aichele, and O. Benson, Fiber-integrated diamond-based single photon-source, *Nano Lett.* **11**, 198 (2010).

- [18] D. Smith, P. Rye, J. Mock, D. Vier, and A. Starr, Enhanced Diffraction from a Grating on the Surface of a Negative-Index Metamaterial, *Phys. Rev. Lett.* **93**, 137405 (2004).
- [19] M. Y. Shalaginov, S. Ishii, J. Liu, J. Liu, J. Irudayaraj, A. Lagutchev, A. Kildishev, and V. Shalaev, Broadband enhancement of spontaneous emission from nitrogen-vacancy centers in nanodiamonds by hyperbolic metamaterials, *Appl. Phys. Lett.* **102**, 173114 (2013).
- [20] M. S. Eggleston, K. Messer, L. Zhang, E. Yablonovitch, and M. C. Wu, Optical antenna enhanced spontaneous emission, *Proc. Natl. Acad. Sci.* **112**, 1704 (2015).
- [21] A. B. Constantine, *Antenna Theory: Analysis and Design*, Microstrip Antennas (John Wiley Sons, New York, 2005), 3rd ed.
- [22] H. A. Wheeler, Fundamental limitations of small antennas, *Proc. IRE* **35**, 1479 (1947).
- [23] J. Dutta, S. A. Ramakrishna, and A. Lakhtakia, Asymmetric coupling and dispersion of surface-plasmon-polariton waves on a periodically patterned anisotropic metal film, *J. Appl. Phys.* **117**, 013102 (2015).
- [24] A. Mohtashami and A. F. Koenderink, Suitability of nanodiamond nitrogen-vacancy centers for spontaneous emission control experiments, *New J. Phys.* **15**, 043017 (2013).
- [25] C. Lu and R. Lipson, Interference lithography: A powerful tool for fabricating periodic structures, *Laser Photon. Rev.* **4**, 568 (2010).
- [26] A. Lakhtakia and R. Messier, *Sculptured Thin Films: Nanoengineered Morphology and Optics* (SPIE Press, Bellingham WA, 2005), Vol. PM143.
- [27] K. Arya, Z. Su, and J. L. Birman, Localization of the Surface Plasmon Polariton Caused by Random Roughness and its Role in Surface-Enhanced Optical Phenomena, *Phys. Rev. Lett.* **54**, 1559 (1985).
- [28] E. Klantsataya, A. François, H. Ebendorff-Heidepriem, B. Sciacca, A. Zuber, and T. M. Monro, Effect of surface roughness on metal enhanced fluorescence in planar substrates and optical fibers, *Opt. Mater. Express* **6**, 2128 (2016).
- [29] I. Abdulhalim, A. Karabchevsky, C. Patzig, B. Rauschenbach, B. Fuhrmann, E. Eltzov, R. Marks, J. Xu, F. Zhang, and A. Lakhtakia, Surface-enhanced fluorescence from metal sculptured thin films with application to biosensing in water, *Appl. Phys. Lett.* **94**, 063106 (2009).
- [30] C. Kurtsiefer, S. Mayer, P. Zarda, and H. Weinfurter, Stable Solid-State Source of Single Photons, *Phys. Rev. Lett.* **85**, 290 (2000).
- [31] M. L. Goldman, A. Sipahigil, M. W. Doherty, N. Y. Yao, S. D. Bennett, M. Markham, D. J. Twitchen, N. B. Manson, A. Kubanek, and M. D. Lukin, Phonon-Induced Population Dynamics and Intersystem Crossing in Nitrogen-Vacancy Centers, *Phys. Rev. Lett.* **114**, 145502 (2015).
- [32] A. Beveratos, R. Brouri, T. Gacoin, J.-P. Poizat, and P. Grangier, Nonclassical radiation from diamond nanocrystals, *Phys. Rev. A* **64**, 061802 (2001).
- [33] F. A. Inam, M. D. Grogan, M. Rollings, T. Gaebel, J. M. Say, C. Bradac, T. A. Birks, W. J. Wadsworth, S. Castelletto, J. R. Rabeau, and J. S. Michael, Emission and nonradiative decay of nanodiamond NV centers in a low refractive index environment, *ACS Nano* **7**, 3833 (2013).
- [34] W. Lukosz and R. E. Kunz, Light emission by magnetic and electric dipoles close to a plane interface. I. Total radiated power, *J. Opt. Soc. Am.* **67**, 1607 (1977).
- [35] M. Kreiter, M. Prummer, B. Hecht, and U. P. Wild, Orientation dependence of fluorescence lifetimes near an interface, *J. Chem. Phys.* **117**, 9430 (2002).
- [36] F. A. Inam, A. M. Edmonds, M. J. Steel, and S. Castelletto, Tracking emission rate dynamics of nitrogen vacancy centers in nanodiamonds, *Appl. Phys. Lett.* **102**, 253109 (2013).
- [37] H. Chew, Radiation and lifetimes of atoms inside dielectric particles, *Phys. Rev. A* **38**, 3410 (1988).
- [38] H. Schniepp and V. Sandoghdar, Spontaneous Emission of Europium Ions Embedded in Dielectric Nanospheres, *Phys. Rev. Lett.* **89**, 257403 (2002).
- [39] M. A. Ordal, R. J. Bell, R. W. Alexander, L. L. Long, and M. R. Querry, Optical properties of fourteen metals in the infrared and far infrared: Al, Co, Cu, Au, Fe, Pb, Mo, Ni, Pd, Pt, Ag, Ti, V, and W, *Appl. Opt.* **24**, 4493 (1985).
- [40] A. F. Koenderink, Single-photon nanoantennas, *ACS Photonics* **4**, 710 (2017).
- [41] A. G. Curto, T. H. Taminiau, G. Volpe, M. P. Kreuzer, R. Quidant, and N. F. Van Hulst, Multipolar radiation of quantum emitters with nanowire optical antennas, *Nat. Commun.* **4**, 1750 (2013).
- [42] S. Schietinger, M. Barth, T. Aichele, and O. Benson, Plasmon-enhanced single photon emission from a nanoassembled metal-diamond hybrid structure at room temperature, *Nano Lett.* **9**, 1694 (2009).
- [43] J. Dutta and S. A. Ramakrishna, Reconfiguring gratings of slanted plasmonic nanocolumns by ion beam irradiation, *Nanotechnology* **26**, 205301 (2015).
- [44] N. H. Wan, B. J. Shields, D. Kim, S. Mouradian, B. Lienhard, M. Walsh, H. Bakhru, T. Schröder, and D. Englund, Efficient extraction of light from a nitrogen-vacancy center in a diamond parabolic reflector, *Nano Lett.* **18**, 2787 (2018).
- [45] J. L. Zhang, S. Sun, M. J. Burek, C. Dory, Y.-K. Tzeng, K. A. Fischer, Y. Kelaita, K. G. Lagoudakis, M. Radulaski, Z.-X. Shen, N. A. Melosh, S. Chu, M. Lonçar, and J. Vučković, Strongly cavity-enhanced spontaneous emission from silicon-vacancy centers in diamond, *Nano Lett.* **18**, 1360 (2018).